# Stress-Intensity Factor and Toughness Measurement at the Nanoscale using Confocal Raman Microscopy

Robert F. Cook, Yvonne B. Gerbig, Jeroen Schoenmaker, Stephan J. Stranick
*National Institute of Standards and Technology, Gaithersburg, USA*

A confocal Raman microscopy technique is presented that allows stress measurement at the nanoscale, which in turn enables measurement of stress-intensity factors (SIF) at crack tips and thus toughness to be estimated. Peak-fitting and high-resolution spatial stepping techniques enable stress resolution of approximately 20 MPa at measurement separations of approximately 100 nm. Micro- and nano-indentation and crack field stress distributions are measured and compared with analytical expressions. The SIF for indentation cracks in Si is shown to be in the range 0.2 MPa $m^{1/2}$ to 0.4 MPa $m^{1/2}$, consistent with chipping-induced indentation stress relief and the toughness of Si.

## 1. Introduction

Among the three modes of accommodating deformation—elastic, plastic, and fracture—quantifying material or structural resistance to these at the nanoscale is least advanced for fracture, despite the fact that fracture is one of the leading detractors of yield and reliability of nanoscale devices [1]. Atomic force microscope methods can measure elastic modulus with approximately 10 nm spatial resolution [2] and instrumented indentation methods can measure modulus and hardness with better than 100 nm resolution [3]. The combination of high-resolution scanning electron microscopy with instrumented indentation techniques employing acute probes enables toughness, $T$, to be measured with approximately 300 nm resolution [4, 5]. The instrumented indentation techniques for nano-scale toughness measurement are an extension of those developed for micro-scale toughness measurement using obtuse (*e.g.*, Vickers) probes [6, 7].

The indentation methods for measuring toughness have in common with macro-scale methods (that employ "fracture mechanics" test specimens) specification of the stress-intensity factor (SIF), $K$ for the system [8]. The SIF characterizes the driving force for fracture and is a function of applied load or displacement, specimen geometry, and crack length. Experiments are performed such that measured values of load, displacement, and crack length, or some combination, can be used to measure the value of $K$ such that the equilibrium condition $K = T$ is met and thus $T$ can be determined. Such methods might be broadly regarded as "exterior" methods of determining toughness as measurements of the boundary conditions of the system are used to specify the state of stress at the crack tip and thus the state of the system relative to equilibrium. Specifically, for linear-elastic systems, the components of stress, $\sigma_{ij}$, near the crack tip are given by [8]

$$\sigma_{ij}(r,\theta) = f_{ij}(\theta)\frac{K}{(2\pi r)^{1/2}} \quad (1)$$

where $r$ and $\theta$ are radial and angular crack-tip coordinates in the cracked material, $f_{ij}$ is an angular function that depends on the stress component, and $K$ depends only on the boundary conditions (which may include the crack length).

An "interior" method of determining toughness is the converse of the above and measures the SIF directly by measuring the stress field near the crack tip in the material to obtain $K$ by inverting Eq. (1):

$$K = \sigma_{ij}(r,\theta)\frac{(2\pi r)^{1/2}}{f_{ij}(\theta)} \quad (2)$$

If the system is known, or assumed, to be in equilibrium then such a direct measurement of $K$ allows $T$ to be determined. Such an approach has been demonstrated using piezospectroscopic techniques, in which an optical response of the material depends on the state of stress, and which, if calibrated, can be used to determine $\sigma_{ij}(r,\theta)$ and thus $K$ from Eq. (2): In this way, fluorescence-based measurements have been used to determine $K$ in $Al_2O_3$ [9], Raman spectroscopy-based measurements have been used to determine $K$ in Si [9], and cathodoluminescence(CL)-based measurements have been used to determine $K$ in GaAs [10] and GaN [11]. These measurements all used Vickers indentations to generate cracks, which should be close to equilibrium with the residual stress field of the elastic-plastic indentation [6 – 8].

Here a high resolution confocal Raman microscopy (CRM) method is used to determine $K$ for Vickers, Berkovich, and cube-corner indentation cracks in Si. The method is first demonstrated on the full residual indentation stress field before focusing attention on the crack-tip stress fields.

## 2. Experimental Method

Two sets of test samples were used in this study: 3 mm thick parallel-sided (001) orientation polished Si disks 35 mm in diameter used in an earlier microindentation study [7] and 500 μm thick parallel-sided (111) disks 25 mm in diameter. The (001) disks were indented with a square Vickers diamond pyramid to a peak load of 2 N with the indentation axes aligned along [110] and $[\bar{1}10]$; the (111) disks were indented with a triangular Berkovich diamond pyramid to peak loads of 400 mN and 30 mN, and with an triangular acute cube-corner indenter to peak loads of 30 mN and 10 mN, in both cases with the indentation axes aligned along $[11\bar{2}]$, $[\bar{2}11]$, and $[1\bar{2}1]$. At these loads, plastic deformation and indentation radial cracks occur with little apparent disruption to the indentation pattern from lateral cracks [7], Figs 1(a) and 2(a). Cartesian coordinate systems were used to

identify the stress coodinates: For the (001) disks, the *z*-axis was taken as normal to the surface, along [001], the *y*-axis in the plane of the surface along $[\bar{1}10]$, and the *x*-axis, in the plane of the surface along [110]; for the (111) disks, the the *z*-axis was taken as normal to the surface, along [111], the *y*-axis in the plane of the surface along $[\bar{1}10]$, and the *x*-axis, in the plane of the surface along $[11\bar{2}]$. In both sets of samples, indentation radial cracks were generated on the secondary {110} cleavage planes of Si [7].

In the CRM method, a Raman spectrum is obtained at each pixel of an analyzed area and the position of the Si Raman peak at ≈ 521 $cm^{-1}$ determined. The position of this peak is compared to that in a reference spectrum obtained from strain-free material and the difference is converted to a stress by a multiplicative constant. Here, CRM data were collected using a custom system: 633 nm wavelength laser radiation was passed through a polarizer and focused on the sample by a high numerical aperture lens to a spot size of ≈ 250 nm. The incident excitation was electrically polarized along $[\bar{1}10]$ (*y*). Scattered Raman light was collected by the lens and passed to a spectrograph. Single-mode optical fibers coupled the laser and spectrograph to the system to provide confocal imaging of the output scattered light. An *x-y* stage with closed-loop control with 10 nm resolution allowed for scanning of the laser; in the experiments here, step sizes between spectrographic measurements varied from ≈ 70 nm to ≈ 300 nm. The information depth for the 633 nm excitation wavelength was 1.3 μm. Stress maps were obtained using *x-y* scans. A Raman spectrum was obtained at each analysis point and the position of the Raman peak determined by center-of-mass or Pearson VII fitting to the data, from which the shift of the peak was found, Figs. 1(b) and 2(b).

For simple stress states (uniaxial, equibiaxial), the Raman shift is positive for a compressive stress state and negative for a tensile stress state, Fig. 1(c): If the spectrum far from the indentation is taken as the reference zero stress state, indicated by "0" in Fig. 1(b), the spectrum adjacent to the residual contact impression ("C") indicates a compressive stress and that adjacent to the radial crack tip ("T") indicates a tensile stress. If the stress state is equibiaxial of magnitude $\sigma_b$, the relationship between the stress components $\sigma_{xx} = \sigma_{yy} = \sigma_b$ and the Raman shift $\Delta\omega$ is [1, 9]

$$\Delta\omega = \frac{2\sigma_b}{\Pi_b} \quad (3)$$

where $\Pi_b$ is the piezospectroscopic coefficient appropriate for the test geometry, in this cases equibiaxial plane stress. For Si, $\Pi_b = -435$ MPa/$cm^{-1}$ [1, 9].

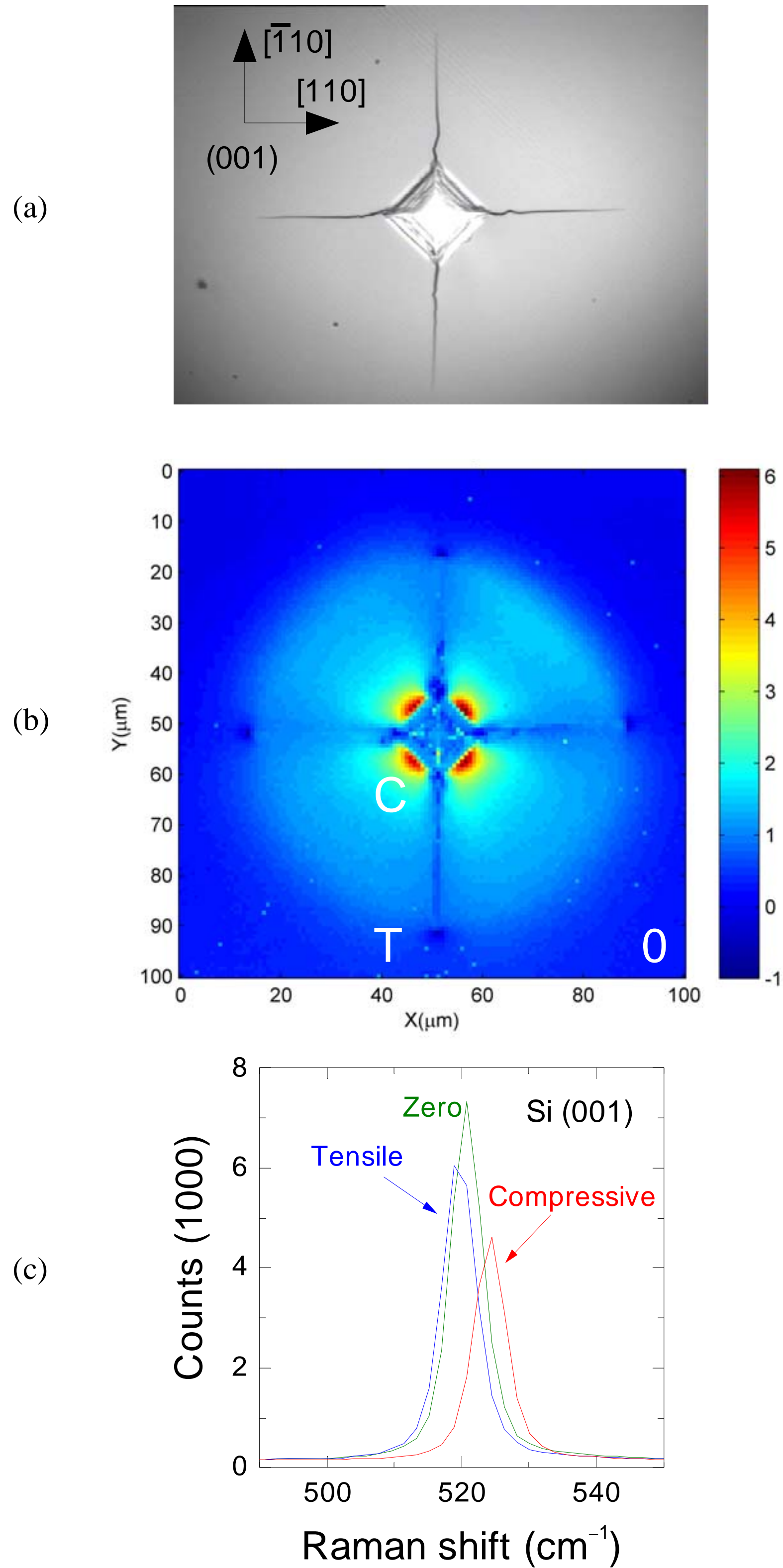


Figure 1. (a) Optical micrograph of a Vickers indentation in Si. (b) Confocal Raman micrograph of the indentation, with the Raman shift indicated. (c) Raman spectra obtained at the points marked in (b).

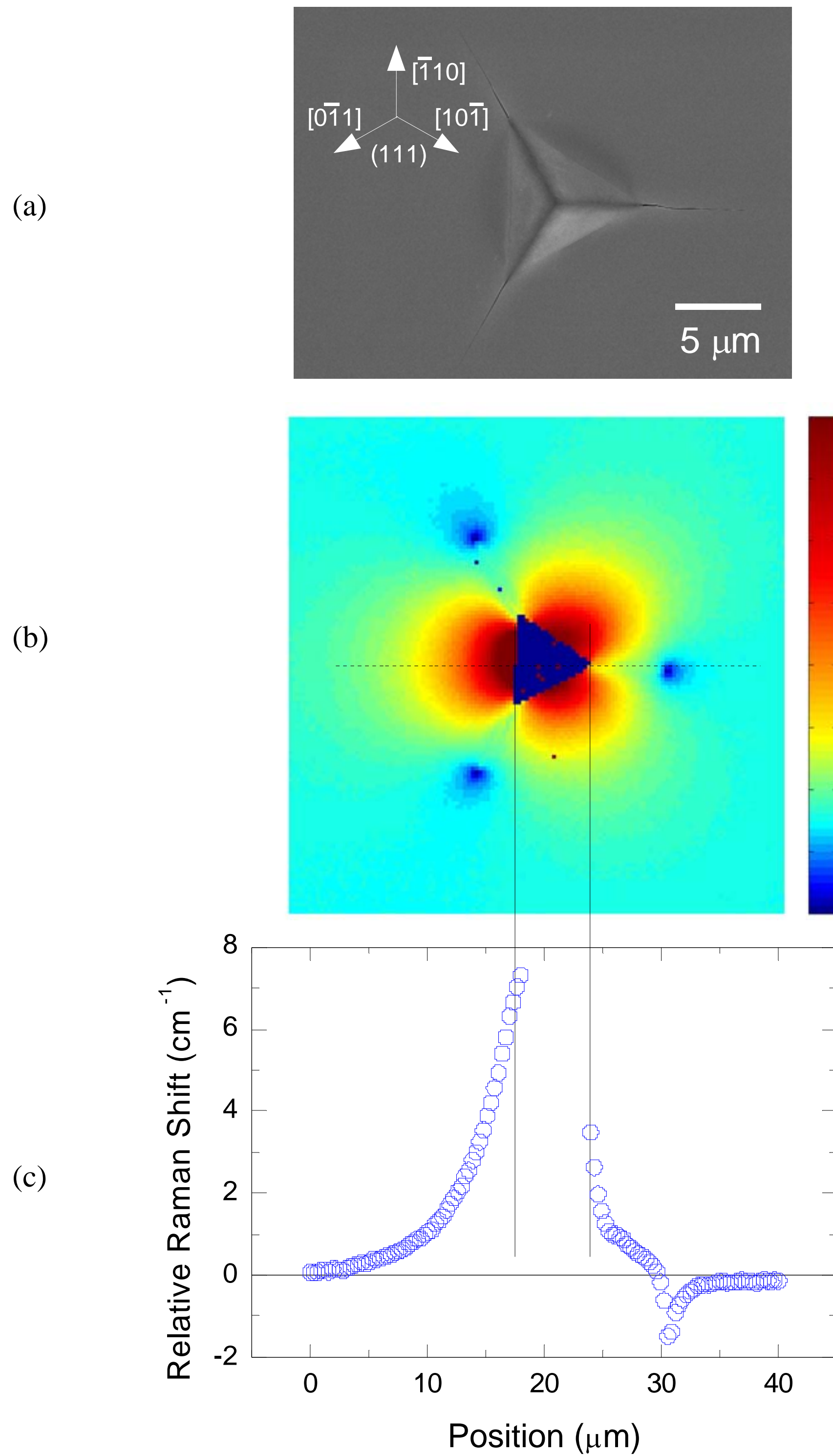


Figure 2. (a) Scanning electron micrograph of a cube-corner indentation in Si. (b) Confocal Raman micrograph of the indentation. (c) Raman shift measured along the dotted line section of (b).

## 3. Results

At the surface of the sample, directly ahead of the radial crack tip, $\theta = 0$ and plane-stress conditions pertain such that $f_{xx} = f_{yy} = 1$. Hence CRM measurements ahead of the crack tip can be simply interpreted as the magnitude of the equibiaxial stress field and the combination of Eqs. (2) and (3) enable the SIF to be measured. Figure 3 shows the Raman shift for the section shown in Fig. 2(c) converted to stress $2\sigma_b$ using Eq. 3; this will be exact for the crack tip stress field, extending from a position of about 30 μm to the right, but only an approximation for the elastic deformation field adjacent to the contact impression extending from a position of about 20 μm to the left. (No useful information is gained within the contact impression extending from a position of 20 μm to 30 μm.)

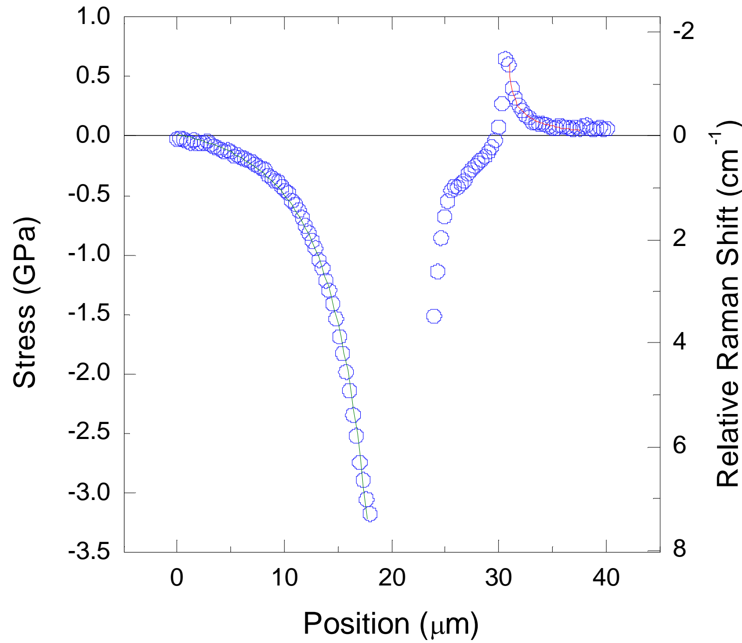


Figure 3. Stress inferred from the shift in the Raman peak for a section through the data along the crack trace in Fig. 2. The solid lines are fits to the data consistent with indentation stress field and crack-tip stress field variations.

The solid line through the elastic stress field (left) data in Fig. 3 is of the form

$$\sigma(\rho) = \sigma_{\text{peak}} (a/\rho)^3 + C \qquad (4)$$

where $\rho$ is an indentation radial coordinate, consistent with the idea that the stress field surrounding an indentation is well-modeled as an expanding spherical cavity [4 – 7, 12]. Here $\sigma_{\text{peak}}$ is the peak stress at the edge of the plastic deformation zone of effective radius $a$; $C$ is a fitting parameter that takes into account the lack of exact knowledge of the baseline zero-stress reference position of the Raman peak. A lower bound on $\sigma_{\text{peak}}$ is $-H$, where $H$ is the hardness. The values for $\sigma_{\text{peak}}$

observed here, approximately 3 GPa, are consistent with the hardness of Si of ≈ 10 GPa.

The solid line through the crack-tip stress field (right) data in Fig. 3 is of the form

$$\sigma(r) = A(r - B)^{-1/2} + C \qquad (5)$$

where $r$ is a radial crack-tip coordinate and $A$, $B$, and $C$ are fitting parameters. Parameters $B$ and $C$ take into account the lack of knowledge of the exact position of the crack tip and the baseline zero-stress reference position of the Raman peak. The spectroscopic shifts and variation of the stress fields adjacent to the indentation impression edge (left of Figs. 2(c) and 3) and along the crack plane and beyond the crack tip (right of Figs. 2(c) and 3) are similar to those measured by Porporati et al. [10] using CL-based methods for Vickers indentations in Si-doped GaAs. The ability of Eqs. (4) and (5) to fit the measurements was also demonstrated in the GaAs study. Comparison of Eqs. (1) and (5) shows that the SIF active at the crack tip is given by $K = (\pi / 2)^{1/2} A$. The SIFs obtained from all the Si indentation measurements are given in Table 1.

Table 1. SIFs of residual indentation cracks {110} in Si.

| **Indenter** | **Peak Load** | **SIF (MPa m$^{1/2}$)** |
|---|---|---|
| Vickers | 2 N | 0.27, 0.34, 0.28, 0. 33, 0.24, 0.38 |
| Berkovich | 400 mN | 0.36, 0.35, 0.28, 0.30 |
| | 30 mN | 0.39 |
| Cube Corner | 30 mN | 0.35 |
| | 10 mN | 0.41 |

## 4. Discussion

The SIF values in Table 1 are approximately the same for all indenter geometries, consistent with the fact that fracture was occurring on the same crystalline plane. In addition, all are less than the value of 0.75 MPa m$^{1/2}$ estimated for the toughness of Si for {110} fracture [7]. The observation here, that residual indentation cracks in Si exhibit SIFs less than the toughness, is consistent with observations at microindentations in Si [7] and with the fact that CRM samples a depth into the material where the crack-tip stress field decreases [9]. The predominant cause, however, is relaxation of the residual indentation stress field during the last stages of indentation unloading, discerned from crack length and strength measurements on microindented Si. Two stress fields compete at the radial position during indentation contact [12]: the reversible contact field, which opposes fracture, and the irreversible residual field, which drives fracture. During unloading, the residual field comes to dominate the contact field and the radial cracks, once initiated, propagate so that $K = T$ is maintained and the cracks maintain an equilibrium length. In the final stages of unloading, above a threshold

peak load, lateral cracks may initiate and propagate as well. Lateral cracks reduce the residual field, by decoupling the plastic deformation zone from the elastically-restraining matrix [13]. Hence, the final indentation configuration for the radial cracks is one of trapped in a sub-equilibrium configuration, $K < T$. Although lateral cracking is not obvious in Figs 1 and 2, other observations suggest lateral cracks are present, but do not lead to associated surface uplift or chipping for 2 N indentations in Si.

The results in Fig. 2(c) and 3, and Table 1 are consistent with those of Zhu et al. [9], albeit with greater spatial and stress resolution. Zhu et al. used a crack-opening displacement method for a larger 10 N {110} indentation crack in Si to determine explicitly the SIF as $K = 0.42$ MPa $m^{1/2}$. This small value, significantly less than the {110} toughness of Si, is consistent with the observation that lateral cracking (and related chipping), and thus post-indentation residual stress relief, increases significantly for indentation loads greater than 2 N in Si. Zhu et al.used a similar method to determine the SIF for radial cracks in (0001) $Al_2O_3$ and obtained $K = 1.2$ MPa $m^{1/2}$, significantly less than the value of 2.5 MPa $m^{1/2}$ observed for fracture perpendicular to [0001]. The image presented by Zhu et al. of an indentation in sapphire exhibits significant lateral cracking. Porporati et al. [10] also used this method to determine the SIF for radial cracks in (001) GaAs and obtained $K = 0.36$ MPa $m^{1/2}$, significantly less than the value of 0.45 MPa $m^{1/2}$ measured for {110} fracture in GaAs. The large indentation load implied by their data similar to Fig. 2(c) ($\approx$ 40 N) suggests that lateral cracking may well have influenced the residual stress field in those measurements as well.

## 5. Conclusions

CRM measurements of stress fields about crack tips in Si are able to measure the SIF. For indentation radial cracks, the SIFs observed were significantly less than the toughness of Si, suggesting substantial relaxation of the residual indentation stress field from the field that existed as the cracks were formed. This direct measurement of the relaxed SIF, as opposed to that inferred from crack-length, strength, or crack-opening displacement measurements, is a critical measure of the behavior of cracks under subsequent, superposed loading. Hence, CRM measurements can be used to identify the concentrations of stress that limit the performance and reliability of nano-scale devices as well as provide quantitative assessment of their behavior under load.

## 6. References

[1] V.T. Srikar, A.K. Swan, M. Selim Ünlü, B. B. Goldberg, and S.M. Spearing, Micro-Raman Measurement of Bending Stresses in Micromachined Silicon Flexures, J. Microelectromechanical Systems 12, (2003) 779-787

[2] G. Stan and R.F. Cook, Mapping the elastic properties of granular Au films by contact resonance atomic force microscopy, Nanotechnology 19 (2008) 235701

[3] W.C. Oliver and G.M. Pharr, An improved technique for determining hardness and elastic modulus using load and displacement sensing indentation experiments, J. Mater. Res. 7 (1992) 1564-1583

[4] D.J. Morris and R.F. Cook, Indentation fracture of low-dielectric constant films, Part I. Experiments and observations, J. Mater. Res. 23 (2008) 2429-2442

[5] D.J. Morris and R.F. Cook, Indentation fracture of low-dielectric constant films, Part II. Indentation fracture mechanics model, J. Mater. Res. 23 (2008) 2443-2457

[6] B.R. Lawn, A.G. Evans, and D.B. Marshall, Elastic/Plastic Indentation Damage in Ceramics: The Median/Radial Crack System, J. Am. Ceram. Soc. 63 (1980) 574-581

[7] R.F. Cook, Strength and Sharp Contact Fracture of Silicon, J. Mat. Sci. 41 (2006) 841-872

[8] B.R. Lawn, Fracture of Brittle Solids-Second Edition, Cambridge University Press, Cambridge, 1993

[9] W. Zhu, K. Wan, and G. Pezzotti, Methods of piezo-spectroscopic calibration of thin film materials: II. Tensile stress field at indentation crack tip, Measurement Sci. Technol. 17 (2006) 191-198

[10] A.A. Porporati, N. Furukawa, W. Zhu, and G. Pezzott, Deformation potentials of Si-doped GaAs from macroscopic residual stress fields J. Appl. Phys. 102 (2007) 083102

[11] W. Zhu, A.A. Porporati, A. Matsutani, N. Lama, and G. Pezzotti, Spatially resolved crack-tip stress analysis in semiconductor by cathodoluminescence piezospectroscopy, J. Appl. Phys. 101 (2007) 103531

[12] R.F. Cook and G.M. Pharr, Direct Observation and Analysis of Indentation Cracking in Glasses and Ceramics, J. Amer. Cer. Soc. 73 (1990) 787-817

[13] R.F. Cook and D.H. Roach, The Effect of Lateral Crack Growth on the Strength of Contact Flaws in Brittle Materials, J. Mat. Res. 1 (1986) 589-600